An investigation into atmospheric nitrous acid (HONO) processes in South Korea

Kiyeon Kim[1], Kyung M. Han[1*], Chul H. Song[1*], Hyojun Lee[1], Ross Beardsley[2], Jinhyeok Yu[1], Greg Yarwood[2], Bonyoung Koo[3], Jasper Madalipay[1], Jung-Hun Woo[4], and Seogju Cho[5]

1. School of Earth Sciences and Environmental Engineering, Gwangju Institute of Science and Technology (GIST), Gwangju 61005, Republic of Korea

2. Ramboll USA, Novato, CA 94945, USA

3. Bay Area Air Quality Management District, San Francisco, CA 94105, USA

4. Department of Technology Fusion Engineering, College of Engineering, Konkuk University, Seoul 05029, Republic of Korea

5. Seoul Metropolitan Government Research Institute of Public Health Environment, 30, Janggunmaeul 3-gil, Gwacheon-si, Gyeonggi-do 13818, Republic of Korea

Short title: Atmospheric HONO processes

* **Corresponding authors:** Kyung Man Han (kmhan@gist.ac.kr) and Chul Han Song

(chsong@gist.ac.kr)

24   **Abstract**

25   Nitrous acid (HONO) is a main precursor of hydroxyl radicals (OH), which contribute

26   to the formation of numerous secondary air pollutants in the troposphere. Despite its

27   importance in atmospheric chemistry, HONO chemistry has not been fully incorporated into

28   many chemical transport models (CTMs). Due to the lack of atmospheric HONO processes,

29   CTM simulations often tend to underestimate atmospheric mixing ratios of HONO. This study

30   was undertaken because simulations with current Community Multiscale Air Quality (CMAQ)

31   model have a strong tendency to underestimate the HONO mixing ratio. In search of missing

32   sources of atmospheric HONO, we attempted to sequentially incorporate the following

33   potential HONO sources and processes into the CMAQ modeling framework: (i) gas-phase

34   HONO reactions; (ii) traffic HONO emissions; (iii) soil HONO emissions; (iv) heterogeneous

35   HONO production on the surfaces of aerosols; (v) heterogeneous HONO formation on tree leaf

36   and building surfaces; (vi) photolysis reactions of particulates and deposited HNO_3/nitrates

37   called 'renoxification'. The simulation performances of the modified CMAQ models were then

38   evaluated by comparing the modeled HONO mixing ratios with the HONO mixing ratios

39   observed at the Olympic Park station in Seoul, South Korea. When HONO processes were fully

40   added to the CMAQ model, average daily HONO mixing ratios increased from 0.06 ppb to

41   1.18 ppb. The daytime HONO mixing ratios produced from the CMAQ model run with a full

42   account of atmospheric HONO processes were found to be in better agreement with

43   observations than those from the original CMAQ model (CMAQv5.2.1) runs with improved

44   statistical metrics (e.g., IOA increased from 0.59 to 0.68, while MB decreased dramatically

45   from -0.57 ppb to -0.34 ppb). In addition, we investigated the contributions of individual

46   atmospheric HONO processes to HONO mixing ratios, as well as the impacts of HONO

47   atmospheric processes on the concentrations of other atmospheric species in South Korea. All

48   these issues are also discussed in this manuscript.

49 **Keywords**: Nitrous acid (HONO); Heterogeneous HONO production; CMAQ model; Ozone
50 production rate.

51 **1. Introduction**

52   Hydroxyl radicals (OH) play a key role in atmospheric chemistry. OH radicals oxidize

53 volatile organic compounds (VOCs), sulfur dioxide (SO_2), and nitrogen dioxide (NO_2),

54 contributing to the formation of secondary organic and inorganic aerosols (Pathak et al., 2009).

55 Therefore, accurate determination of the mixing ratio of OH radicals is crucial to understanding

56 atmospheric photochemistry in both polluted and remote areas.

57   Nitrous acid (HNO_2 or HONO) has been recognized as a main precursor of OH radicals

58 via photo-dissociation (R1) (Alicke et al., 2003; Harris et al., 1982; Kleffmann et al., 2005):

59        $HONO + hv \xrightarrow{j_{HONO}}$ OH + NO (300 nm < λ < 405 nm)   (R1)

60 Several studies have estimated that HONO photolysis reactions contribute 20 – 80% of OH

61 radicals and 30 – 87% of HO_x formation in polluted urban areas (Acker et al., 2006; Alicke et

62 al., 2003; Hendrick et al., 2014; Kim et al., 2014; Kleffmann et al., 2005; Monks et al., 2009;

63 Ren et al., 2003). However, it was also recognized that the HONO chemistry was not yet fully

64 understood.

65   Therefore, many field measurements have been carried out to characterize atmospheric

66 HONO processes (Kim et al., 2014; Lee et al., 2016; Li et al., 2012; Su et al., 2008). These

67 studies showed that the observed HONO mixing ratios were significantly higher than those

68 predicted by atmospheric chemistry-transport model simulations (Lee et al., 2016; Li et al.,

69 2014; Su et al., 2008; VandenBoer et al., 2013). This indicates that there should be missing

70 HONO sources or processes that are not considered in current atmospheric models (CTMs).

71   Recent studies have proposed incorporating several HONO production pathways into

72 chemical transport models to explain the missing HONO processes. Suggested sources include

73 i) traffic HONO emissions (Czader et al., 2015; Kirchstetter et al., 1996; Kurtenbach et al.,

74 2001; Li et al., 2018; Nakashima and Kajii, 2017; Rappenglück et al., 2013; Xu et al., 2015);

75   ii) soil HONO emissions (Meusel et al., 2016; Nagai and Kubota, 1972; Oswald et al., 2013;

76   Weber et al., 2015); iii) HONO emissions from biomass burning (Cheng et al., 2014; Crutzen

77   and Andreae, 1990; Nie et al., 2015); iv) indoor HONO emissions (Gligorovski, 2016; Zhang

78   et al., 2019); and iv) heterogeneous conversion of NO_2 to HONO on the surfaces of aerosols,

79   grounds, and leaves (Han et al., 2017; Reisinger, 2000; Svensson et al., 1987; Stemmler et al.,

80   2016; Wiesen et al., 1995).

81   Among these processes, traffic HONO emissions were reported to be the key factor

82   influencing the HONO mixing ratio in the Beijing–Tianjin–Hebei (BTH) region at night

83   (Zhang et al., 2019). Heterogeneous NO_2 reactions on aerosol surfaces were an important

84   source of HONO during the severe haze period in Beijing (Jia et al., 2020). On the other hand,

85   Zhang et al. (2016) reported that heterogeneous reactions on ground surfaces could be the

86   dominant source of atmospheric HONO, accounting for ~42% of the HONO mixing ratios in

87   Hong Kong suburban areas.

88   These findings may indicate that atmospheric HONO production and a potential cause

89   of discrepancies between modeled and observed HONO mixing ratios may vary temporally

90   and regionally. In addition, no research has been conducted on which sources of HONO control

91   the levels of HONO in Seoul, South Korea. In this context, the aims of this study are three-fold:

92   i) to determine which HONO sources or processes are significant in South Korea; ii) to estimate

93   the budget of the HONO mixing ratios from various HONO sources; and iii) achieving

94   objectives i) and ii) to develop a near-perfect CTM in terms of HONO mixing ratio. To

95   accomplish these goals, we decided to improve the US EPA CMAQ v5.2.1 model by

96   incorporating several HONO production pathways including i) homogeneous HONO reactions;

97   ii) direct HONO emissions from biomass burning, traffic vehicles, and soil; iii) heterogeneous

98   HONO production on the surfaces of atmospheric aerosols, buildings, and tree leaves; and iv)

99   photolysis reactions of particulate and deposited HNO_3/nitrate (renoxification).

100   We then tested the performances of the modified CMAQ models by comparing the

101   modeled HONO mixing ratios with the HONO mixing ratios observed during the Korea-United

102   States Air Quality (KORUS-AQ) campaign. After the comparison analysis, we evaluated the

103   contributions of individual HONO processes to the HONO budget in South Korea and also

104   investigated the effects of the HONO mixing ratios on the levels of other important atmospheric

105   species.

106   **2. Methodology**

107   In this study, we incorporated various HONO sources and reactions into the CMAQ

108   model framework to accurately estimate HONO mixing ratios in the atmosphere. Then, the

109   simulation results of the modified CMAQ models were analyzed, comparing the modeled

110   outputs with observations during the KORUS-AQ campaign. Details of the modifications of

111   CMAQ models, the HONO measurements, and potentially important HONO sources

112   considered in this study are described in the following sections.

113   **2.1. WRF-CMAQ model configuration**

114   Simulation of the Community Multiscale Air Quality (CMAQ) v5.2.1 model (Byun

115   and Schere, 2006) was carried out to estimate the HONO mixing ratios during the period of the

116   KORUS-AQ campaign (9 May – 12 June, 2016). Figure 1 shows the horizontal domain (A1)

117   for the CMAQ model simulation. The spatial domain has 273×204 grid cells with a horizontal

118   resolution of 15×15 km^2 and contains 15 vertical layers with the first layer at ~34 m above

119   the ground.

120   The photochemical mechanism used in the simulation of the CMAQ model was the

121   Statewide Air Pollution Research Center-07 (SAPRC-07 TC) (Carter, 2010; Hutzell et al.,

122   2012). The AERO6 module was used for aerosol calculations (Binkowski and Roselle, 2003).

123   In particular, the heterogeneous reactions considered in this study were embedded into the

124 SAPRC-07 TC via the Korean Flexible Chemistry (KFC) editor. The KFC editor is a chemical

125 mechanism editor in a framework of Graphic User Interface (GUI) developed to quickly

126 implement the modifications of the chemical mechanisms of the CMAQ model. The details of

127 the heterogeneous reactions we considered are discussed in Sects. 2.3.5 – 2.3.6.

128   The Weather Research and Forecasting (WRF) v3.8.1 model (Skamarock et al., 2008)

129 was run to generate meteorological fields that drive the CMAQ model. The physical options

130 used in the WRF run are as follows: i) WRF Single-Moment 6-class Microphysics scheme

131 (Hong and Lim, 2006); ii) Rapid radiative transfer model (RRTMG) for longwave and

132 shortwave radiation (Iacono et al., 2008); iii) the NOAH Land Surface scheme (Chen and

133 Dudhia, 2001); iv) Yonsei University (YSU) Planetary Boundary Layer (PBL) scheme (Hong

134 et al., 2006); v) MM5 surface layer scheme (Jiménez et al., 2012); and vi) the Grell-Freitas

135 Ensemble scheme for cumulus physics (Grell and Freitas, 2014). Initial and boundary

136 conditions for the WRF model runs were obtained from the National Center for Environmental

137 Prediction Final Analysis (NCEP-FNL) every six hours.

138   For anthropogenic emissions, this study used the KORUS v5.0 inventory processed by

139 the Sparse Matrix Operator Kernel Emissions in Asia (SMOKE-Asia; Woo et al., 2012) (Woo

140 et al., 2020). The KORUS v5.0 emissions were developed particularly for CTM runs as part of

141 the KORUS-AQ campaign. Biogenic emissions were generated using the Model of Emissions

142 of Gases and Aerosol from Nature (MEGAN) v2.10 (Guenther et al., 2012). Fire emissions

143 were obtained from the Fire Inventory from NCAR (FINN) v1.5 emission inventory

144 (https://bai.acom.ucar.edu/Data/fire/; Wiedinmyer et al., 2011). The various HONO emissions

145 considered in this study are discussed in Sects. 2.3.2. – 2.3.4.
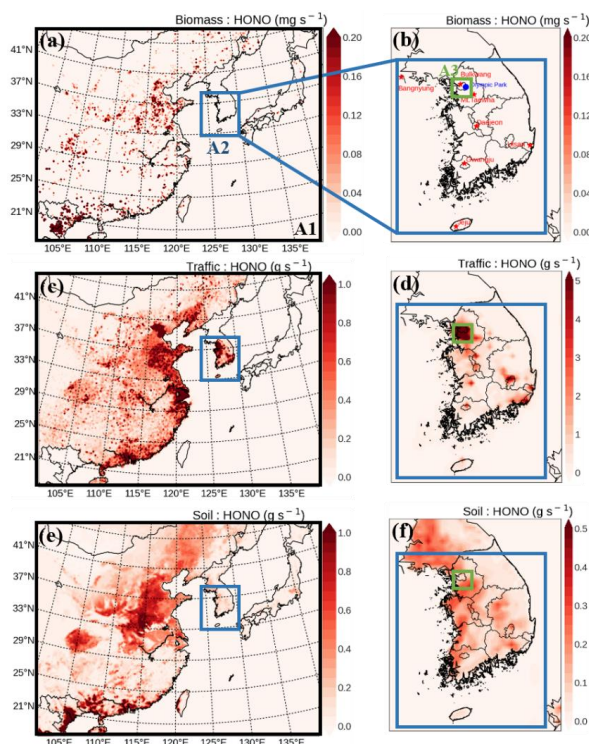
146

147 **Figure 1.** Spatial distributions of HONO emission rates from biomass burning (panels (a) and
148 (b)), from traffic (panels (c) and (d)), and from soil (panels (e) and (f)) over East Asia (A1),
149 South Korea (A2), and the Seoul Metropolitan Area (A3). Several super-monitoring stations
150 are located at Bangnyung-Do, Bulkwang-Dong, Olympic Park, Mt.Taehwa, Daejeon, Gwangju,
151 Ulsan, and Jeju. The locations of these super-stations are shown in panel (b).

152 **2.2 Measurements**

153   During the KORUS-AQ campaign period, concentrations of NO_2, O_3, and particulate

154 matter were measured at several locations such as Olympic Park (37.52N; 127.12E),

155 Bangnyung (37.96N; 124.64E), Bulkwang (37.61N; 126.93E), Mt. Taewha (37.31N; 127.31E),

156 Daejeon (36.35N; 127.38E), Gwangju (35.23N; 126.84E), Ulsan (35.53N; 129.31E), and Jeju

157 (33.32N; 126.40E) (refer to Fig. 1b regarding the locations). In this study, we also used data

158 observed   at   approximately   320   stations   from   the   AIR-KOREA   network

159 (https://www.air.korea.or.kr), officially managed by the Korean Ministry of Environment in

160 South Korea.

161   Surface data observed at the Olympic Park station in Seoul were used for direct comparisons

162   between simulated and observed HONO mixing ratios. These HONO mixing ratios were

163   measured using the Monitor for AeRosols and GAses in ambient air (MARGA ADI 2080)

164   (Applikon-ECN, Netherlands) instrument with a time resolution of 1 hour. This measurement

165   is based on the wet-denuder-ion-chromatography (WD/IC) method. In the WD/IC system,

166   HONO molecules absorbed by the solution in the denuder were converted to nitrite (NO_2^-),

167   and then the nitrite concentrations were quantified by ion chromatography (Xu et al., 2019).

168   The detection limit of the MARGA instrument for HONO is ~0.02 ppb. At the Olympic Park

169   station, NO_2 and O_3 were also measured using commercially available instruments, EC9841

170   and EC9810, respectively, manufactured by Ecotech. Their detection limits for both species

171   are ~0.5 ppb during the daytime. Details on the principles of EC9841 and EC9810 can be

172   found in Keywood et al. (2019). $PM_{2.5}$ at the Olympic Park station were measured

173   continuously using a Thermo Scientific Continuous Particulate Monitor, FH62C14, based on

174   the beta attenuation method. The detection limit of the instrument is $4\mu g/m^3$ in hourly

175   measurements. Further information about instruments is provided in Table S1.

176   Meteorological data on temperature, relative humidity, pressure, wind speeds, and

177   wind directions were also measured by the Automated Synoptic Observing System (ASOS) at

178   the Olympic Park station. In order to test the simulation performances of the WRF-CMAQ

179   model, observed meteorological data was compared with the modeled outputs, which is shown

180   in Table S2. In general, WRF model simulations tended to accurately predict meteorological

181   fields.

182   **Table 1.** Comparison of parameterizations of HONO processes between CMAQ v5.2.1 and this study.

	HONO processes	CMAQ v5.2.1	This study	Ref.
	(R1) $HONO + h\nu \xrightarrow{J_{HONO}} OH + NO$	J_{HONO}	J_{HONO}	1
	(R2) $NPHE + h\nu \xrightarrow{J_{NPHE}} HONO + xPROD2$	$J_{NPHE} = 1.50e^{-3} \times J_{NO_2}$	$J_{NPHE} = 1.50^{-3} \times J_{NO_2}$	
	(R3) $OH + NO + M \xrightarrow{k_3} HONO$	$k_3 = \{\frac{k_a[M]}{(1+k_a[M]/k_b)}\}0.6^{\frac{1}{1+[log_{10}(\frac{k_a[M]}{k_b})]^2}}$ $\bullet\ k_a = 7.0\times 10^{-31}(\frac{T}{300})^{-2.6},$ $\bullet\ k_b = 3.6\times 10^{-11}(\frac{T}{300})^{-0.1}$	$\bullet\ k_a = 7.1\times 10^{-31}(\frac{T}{300})^{-2.6},$ $\bullet\ k_b = 3.6\times 10^{-11}(\frac{T}{300})^{-0.1}$	2
	(R4) $HONO + OH \xrightarrow{k_4} H_2O + NO_2$	$k_4 = 2.5\times 10^{-12} e^{(\frac{-260}{T})}$	$k_4 = 3.0 \times 10^{-12} e^{(\frac{-250}{T})}$	
Reaction	(R5) $2NO_2 + H_2O \xrightarrow{k_{aerosol}} HONO + HNO_3$	$k_{aerosol} = 1.0 \times 10^{-4}(S/V)$	$k_{aerosol} = \frac{1}{4} v_{NO_2}(S/V) \times \gamma_{a\_NO_2}$ Daytime: $\gamma_{a\_NO_2} = 1.3 \times 10^{-4} \times \frac{\text{light intensity}}{900(W \cdot M^{-2})}$ Nighttime: $\gamma_{a\_NO_2} = 8.0 \times 10^{-6}$	3, 4 / 5
	(R6) $2NO_2 + H_2O \xrightarrow{k_{ground}} HONO + HNO_3$	$k_{ground} = 5.0 \times 10^{-5} \times (\frac{S_{g,building}}{V} + \frac{S_{g,leaf}}{V})$ $\bullet\ \frac{S_{g,leaf}}{V} = \frac{2\times LAI}{H}$ $\bullet\ \frac{S_{g,building}}{V} = PURB \times \frac{0.2\frac{m^2}{m^3}}{100\%}$	$k_{ground} = \frac{1}{8} \times v_{NO_2} \times \gamma_{g\_NO_2} \times (\frac{S_{g,building}}{V} + \frac{S_{g,leaf}}{V})$ $\bullet\ \frac{S_{g,leaf}}{V} = \frac{2\times LAI}{H}$ $\bullet\ \frac{S_{g,building}}{V} = PURB \times \frac{0.3\frac{m^2}{m^3}}{100\%}$ Daytime: $\gamma_{g\_NO_2} = 5.8 \times 10^{-6} \times \frac{\text{light intensity}}{900(W \cdot M^{-2})}$ Nighttime: $\gamma_{g\_NO_2} = 5.0 \times 10^{-7}$	6 / 7 / 4, 8 / 9
	(R7) $pNO_3 + h\nu \xrightarrow{J_{pNO_3}} 0.67HONO + 0.33NO_2$	-	$J_{pNO_3} = 118 \times J_{HNO_3}$	
	(R8) Deposited HNO_3/nitrate + hν $\xrightarrow{J_{D\_HNO_3/nitrate}} 0.67HONO + 0.33NO_2$	-	$J_{D\_HNO_3/nitrate} = 48 \times J_{HNO_3}$	10
	Biomass Burning	-	FINNv1.5	11
Emission Traffic		-	Gasoline: $HONO_{traffic}/NO_x = 0.8\%$ Diesel: $HONO_{traffic}/NO_x = 2.3\%$	7
Soil		-	$HONO_{soil}/NO_x = f(\text{soil water content})$	12

1. Burkholder et al. (2015); 2. Burkholder et al. (2020); 3. Xue et al. (2022); 4. Czader et al. (2012); 5. Vandenboer et al. (2013); 6. Sarwar et al. (2008); 7. Zhang et al. (2016); 8. Yu et al. (2021); 9. Yu et al. (2022); 10. Fu et al. (2019); 11. Wiedinmyer et al. (2011); 12. Mensel et al. (2018)

183

184 **2.3 HONO sources**

185   In this study, we considered several possible missing HONO sources or processes in

186 the CMAQ model simulations. The possible missing HONO sources include gas-phase HONO

187 reactions, three HONO emission sources, three heterogeneous HONO reactions, and two

188 photolytic reactions. The considered possible missing HONO sources are also contrasted to the

189 current HONO processes embedded in the CMAQ v5.2.1 model in Table 1. The details of each

190 HONO process are discussed below.

191 **Table 2.** Design for 8 EXP simulations.

HONO Source	Experiment							
	EXP1	EXP2	EXP3	EXP4	EXP5	EXP6	EXP7	EXP8
GAS[1]	√	√	√	√	√	√	√	√
BioB[2]		√	√	√	√	√	√	√
TRAF[3]			√	√	√	√	√	√
SOIL[4]				√	√	√	√	√
HET_A[5]					√	√	√	√
HET_L[6]						√	√	√
HET_BD[7]							√	√
RENO$_x$[8]								√

192 [1] Gas-phase reactions; [2] Biomass Burning Emissions; [3] Traffic Emissions; [4] Soil Emissions; [5] Heterogeneous reactions on
193 aerosol surfaces; [6] Heterogeneous reactions on the surfaces of leaves; [7] Heterogeneous reactions on the surfaces of buildings;
194 [8] Renoxification

195 **2.3.1 Gas Phase reactions (GAS)**

196   We used the SAPRC-07 TC chemical mechanism as base mechanism. A total of 4 gas-

197 phase HONO-related reactions were considered for HONO formation and dissociation (Carter,

198 2010;). HONO is produced by i) photolysis of nitrophenol (NPHE) (R2) and ii) reaction of

199 NO with OH in the presence of the third body (M) (R3). Meanwhile, HONO is removed by

200 reaction with OH radicals (R4) and photolytic dissociation (R1). All these reactions are shown

201 below:

202 $$NPHE + hv \xrightarrow{j_{NPHE}} HONO + xPROD2 \tag{R2}$$

203 $$OH + NO + M \xrightarrow{k_3} HONO \tag{R3}$$

204 $$HONO + OH \xrightarrow{k_4} H_2O + NO_2 \qquad (R4)$$
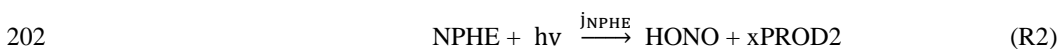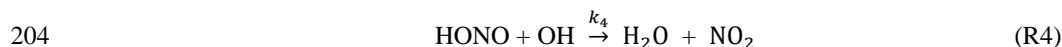
205 where, J_{NPHE} (R2) and J_{HONO} (R1) are the photolysis rates constants of NPHE and HONO,

206 respectively, which were adopted from the study of Stockwell et al. (1990). As shown in Table

207 1, J_{NPHE} was calculated, based on J_{NO2} (i.e., $J_{NPHE} = 1.50 \times 10^{-3} \times J_{NO2}$). k_3 and k_4 are the

208 reaction rate constants of (R3) and (R4) and were obtained from the National Aeronautics and

209 Space Administration (NASA) Jet Propulsion Laboratory (JPL) Publication 19 (Burkholder et

210 al., 2020). Among these reactions, the reaction rate constants of (R3) and (R4) were updated in

211 our study (refer to Table 1). The effect of these gaseous reactions on HONO mixing ratios was

212 tested in the EXP1 simulation (see GAS in Table 2).

2.3.2 Biomass burning emissions (BioB)

214 Biomass combustion includes three types of burning events: natural wildfires,

215 agricultural fires, and wood burning (Wiedinmyer et al., 2011). In East Asia, agricultural fires

216 typically occur in early summer and fall (Ryu et al., 2004; Tao et al., 2013; Zhang et al., 2013).

217 The period of the KORUS-AQ campaign coincides with the period of the agricultural residue

218 burning after barley and wheat harvest in East Asia. Biomass burning emissions, including

219 agricultural fire emissions, were obtained from the Fire INventory from NCAR version 1.5

220 (FINN v1.5, Wiedinmyer et al., 2011; Wiedinmyer et al., 2006). This was then considered in

221 the EXP2 simulation (see BioB in Table 2). The spatial distributions of HONO emissions from

222 the biomass burning events in the East Asia domain (A1), South Korea domain (A2), and Seoul

223 Metropolitan Area domain (A3) are presented in Fig. 1a and 1b. However, we found that the

224 HONO emission rates used in the EXP2 simulation were relatively small, compared to the total

225 HONO emission rates presented in Fig. 1 and Table 3.

226

227

Table 3. HONO emission rates from biomass burning, traffic, and soil. The total HONO emission rates during the period of the KORUS-AQ campaign are shown.

Region	Source			
	Biomass Burning Emission $(g \cdot s^{-1})$	Traffic Emission $(Mg \cdot s^{-1})$	Soil Emission $(Mg \cdot s^{-1})$	Total $(Mg \cdot s^{-1})$
East Asia (A1)	2.46	6.40	5.65	14.51
South Korea (A2)	0.00	0.32	0.06	0.38
Seoul Metropolitan Area (A3)	0.00	0.10	0.01	0.1

2.3.3 Traffic emissions (TRAF)

Traffic emissions are an important HONO source, particularly at night (Zhang et al., 2016). HONO is emitted directly from vehicle exhaust systems. In this study, to estimate the direct HONO emissions from traffic sources, we assumed that the HONO to NO_x emission ratio is 0.8% for gasoline vehicles and 2.3% for diesel vehicles (Sarwar et al., 2008; Zhang et al., 2016). All off-road vehicles were treated as diesel vehicles in the calculations of HONO emissions (Gutzwiller et al., 2002). Table 3 presents the total emission rates for East Asia, South Korea, and the Seoul Metropolitan Area, which are 6.40, 0.32, and 0.1 Mg s^{-1}, respectively. Moreover, as shown in Fig. 1c and 1d, HONO emissions from traffic sources are dominant, particularly in metropolitan areas such as Seoul, Beijing, Shanghai, and Hong Kong. The contribution of traffic sources to total HONO emissions was estimated to be dominant in the Seoul Metropolitan Area. In the EXP3 simulation, the impact of the traffic source (see TRAF in Table 2) on the atmospheric HONO mixing ratios was investigated.

2.3.4 Soil emissions (SOIL)

Emissions from soil bacterial activity are important sources of HONO. The amount of their emissions depends on the soil type, land category, fertilization, temperature, soil water content (SWC in %), and soil pH (Meusel et al., 2018; Wu et al., 2020). In this study, HONO

247   emissions were estimated based on the ratio of HONO to NO_x emissions from soil (Oswald et

248   al., 2013). SWC was used as a proxy for soil pH due to the technical limitations of direct

249   measurement of the soil pH. The SWCs were set at 0-7.5%, 7.5-15%, 15-20%, 20-30% and 30-

250   40% for HONO-to-NO_x ratios of 1.0, 0.67, 0.75, 0.5 and 0.25, respectively, because the ratio

251   of HONO to NO_x is very sensitive to the water content in the soil. For this estimation, monthly

252   soil NO_x emissions were acquired from the MEGAN v2.10 model.

253   The HONO emission rate from soil was estimated at 0.06 Mg s^{-1} for South Korea,

254   accounting for ~16% of the total HONO emission rate in South Korea (refer to Table 3). The

255   spatial distributions of emission are presented in Fig. 1e and 1f. The impact of HONO soil

256   emissions (see SOIL in Table 2) was examined in the EXP4 simulation.

257   **2.3.5 Heterogeneous reaction of NO_2 on atmospheric aerosol surfaces (HET_A)**

258   In the EXP5 simulation, we added the heterogeneous reaction of NO_2 on the surface of

259   atmospheric aerosols via reaction (R5) (see HET_A in Table 2), which has been reported to be

260   a possible pathway for HONO formation (Han et al., 2017; Lu et al., 2018; Reisinger, 2000;

261   Svensson et al., 1987; Wiesen et al., 1995).

262                     $$2NO_2 + H_2O \xrightarrow{k_{aerosol}} HONO + HNO_3$$ (R5)
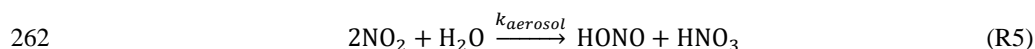
263   We found a similar diurnal pattern of the concentration ratio of HONO/NO_2 to the

264   HONO mixing ratio at the Olympic Park station. This indicates that the conversion of NO_2 to

265   HONO via reaction (R5) may be a main process for HONO formation (Fig. S1). The

266   HONO/NO_2 ratios at the Olympic Park station in Seoul ranged from 1.9% to 6.8% during the

267   KORUS-AQ campaign, which is also comparable to those observed in Taichung, Taiwan, and

268   Shanghai, China (Hao et al., 2020; Tong et al., 2015).

269   The current AERO6 module in the CMAQv5.2.1 model already considers reaction (R5)

270   but does not take into account 'photo-enhancement'. However, several previous studies

271   suggested that the photo-enhanced reactions should produce more HONO molecules during the

272   daytime (Colussi et al., 2013; Czader et al., 2012; Fu et al., 2019; Levy et al., 2014; Li et al.,

273   2010; Sarwar et al., 2008). The potential photo-enhancement of the reaction (R5) was taken

274   into account by making $k_{aerosol}$ dependent on the magnitude of light intensity:

275    $$k_{aerosol} = \frac{1}{4} \times v_{NO_2} \times \frac{S_{aero}}{V} \times \gamma_{a,NO_2} \qquad (Eq.1)$$

276    $$\gamma_{a,NO_2} = 8.0 \times 10^{-6} \quad (nighttime)$$

277    $$\gamma_{a,NO_2} = 1.3 \times 10^{-4} \times (\frac{light\ intensity}{900}) \quad (daytime)$$

278   where, v_{NO_2}, $\frac{S_{aero}}{V}$, and γ_{a,NO_2} represent the mean molecular velocity of NO_2 ($m \cdot s^{-1}$), the

279   aerosol surface density ($m^2 \cdot m^{-3}$), and the NO_2 uptake coefficient on the surface of

280   atmospheric aerosols, respectively. It should also be noted in Table 1 that the CMAQ v5.2.1

281   model simply uses a fixed reaction constant (= $10^{-4} \times \frac{S_{aero}}{V}$) for this heterogeneous reaction.

282   **2.3.6 Heterogeneous reactions of NO₂ on tree leaf and building surfaces (HET_L and**

283   **HET_BD)**

284   The heterogeneous reaction of NO₂ can also take place on the ground surfaces (e.g.,

285   tree leaves and buildings). Several studies have reported that heterogeneous reactions on the

286   surfaces of tree leaves and buildings via reaction (R6) can contribute to the HONO mixing

287   ratios in the atmosphere (An et al., 2013; Hou et al., 2016; Karamchandani et al., 2015; Zhang

288   et al., 2016). Therefore, we also considered these photo-enhanced heterogeneous NO₂ reactions.

289    $$2NO_2 + H_2O \xrightarrow{k_{L\&B}} HONO + HNO_3 \qquad (R6)$$
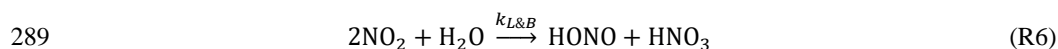
290   In this study, $k_{L\&B}$ was calculated using equation (2), with a modification of the equation:

291    $$k_{L\&B} = \frac{1}{8} \times v_{NO_2} \times \gamma_{g,NO_2} \times (\frac{S_{g,building}}{V} + \frac{S_{g,leaf}}{V}) \qquad (Eq.2)$$

292    $$\gamma_{g,NO_2} = 5.0 \times 10^{-7} \quad (nighttime)$$

293    $$\gamma_{g,NO_2} = 5.8 \times 10^{-6} \times (\frac{light\ intensity}{900}) \quad (daytime)$$

294   where γ_{g,NO_2} is the NO_2 uptake coefficient on the ground surfaces. Here, $\frac{S_{g,building}}{V}$

295   represents the ratios of the building surface area to the volume, which were calculated from

296   equation (3):

$$\frac{S_{g,building}}{V} = PURB \times \frac{0.3\frac{m^2}{m^3}}{100\%} \qquad (Eq.3)$$

298   where, PURB represents the percentage of building area with a maximum value of 0.3

299   (Kurtenbach et al. 2001). For vegetation areas, $\frac{S_{g,leaf}}{V}$ (the ratio of the leaf surface to volume)

300   was estimated based on leaf area index (LAI) information, along with equation (4) proposed

301   by Sarwar et al. (2008):

$$\frac{S_{g,leaf}}{V} = \frac{2 \times LAI}{H} \qquad (Eq.4)$$

303   where, H represents the height of the first layer of the model simulation (Sarwar et al., 2008;

304   Yuan et al., 2011; Zhang et al., 2012). The LAI was obtained from improved Moderate

305   Resolution Spectroradiometer (MODIS) land use data (Yuan et al., 2011).

306   **2.3.7. Photolysis reactions (RENO$_x$)**

307   Several measurement studies have reported that the photolytic dissociation of

308   particulate nitrate (pNO$_3$) in the atmosphere (R7) may be able to explain the high HONO

309   mixing ratios observed during the daytime (Romer et al., 2018; Ye et al., 2017). Other studies

310   suggested that the photolysis reactions of HNO$_3$ and nitrate deposited on tree canopies and

311   artificial surfaces (R8) can also be significant sources of daytime HONO, particularly in rural

312   areas (Ye et al., 2016; Zhou et al., 2011). All these heterogeneous reactions from N(V) to N(III)

313   or N(IV) are called atmospheric 'renoxification'. Some studies have also reported that these

314   types of reduction reactions actually take place in the snow (Chen et al., 2019). In order to

315   better estimate the daytime mixing ratios of HONO in the atmosphere, reactions (R7) and (R8)

316   were included in the EXP8 simulation (see RENO$_x$ in Table 2).

317 $$pNO_3 \xrightarrow{h\nu} 0.67 \ HONO + 0.33 \ NO_2 \qquad \text{(R7)}$$

318 $$deposited\_HNO_3/nitrate \xrightarrow{h\nu} 0.67 \ HONO + 0.33 \ NO_2 \qquad \text{(R8)}$$
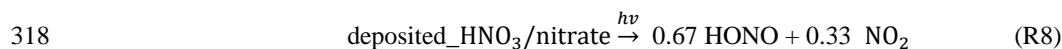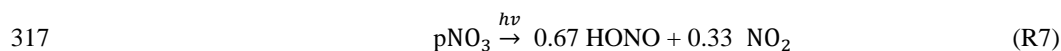
319 In the EXP8 simulation, we chose equations for both the photolysis rate constant of particulate

320 NO_3^- (denoted by J_{pNO_3}) and the photolysis rate constant of HNO_3/nitrate deposited on

321 surfaces (denoted by $J_{D\_HNO_3/nitrate}$), following the methods proposed by Zhang et al. (2022),

322 and Fu et al. (2019). These equations are presented below:

323 $$J_{pNO_3} = 118 \times J_{HNO_3} \qquad \text{(Eq.5)}$$

324 $$J_{D\_HNO_3/nirate} = 48 \times J_{HNO_3} \qquad \text{(Eq.6)}$$

325 where, J_{HNO_3} is the reaction rate constant of gaseous HNO_3 photo-dissociation, which is

326 calculated by the photolysis rate preprocessor module (JPROC) in the CMAQ model.

327 **3. Results and Discussions**

328 In this section, we first evaluated the performances of the modified CMAQ models in

329 terms of HONO mixing ratios by comparing the model outputs with ground-based observations

330 from the Olympic Park station in South Korea. We then carried out sensitivity tests to estimate

331 the contributions of the various atmospheric HONO processes to atmospheric HONO mixing

332 ratios.

333 **3.1 Observed vs Simulated HONO mixing ratios**

334 Figure 2 presents the hourly variations of the HONO mixing ratios at the Olympic Park

335 station. Observations are marked with open black circles, and colored lines represent HONO

336 mixing ratios calculated from the 8 EXP simulations. When HONO sources were added

337 sequentially to the experiments, the HONO mixing ratios averaged over the entire simulation

338 period increased from 0.06 ppb (EXP1 simulation) to 1.18 ppb (EXP8 simulation). The

339 averaged HONO mixing ratios in the EXP8 simulation, which took into account all the HONO

340 processes, were almost comparable to those observed from the ground (1.35 ppb of HONO).

341   The CMAQ-simulated HONO mixing ratios were particularly underestimated from 19

342   May to 23 May, 2016 (refer to gray-shadow period in Fig. 2). This period was characterized

343   by low wind speeds and poor mixing within planetary boundary layer height (PBLH), which

344   can lead to the accumulation of air pollutants (Crawford et al., 2021). On the other hand, the

345   WRF model has a strong tendency to produce higher wind speeds than the actual ones, which

346   may lead to underestimation of air pollutant concentrations (Jo et al., 2017). Therefore, the

347   underestimation of the HONO mixing ratios may be caused by the overestimation of the wind

348   speed on a given period. Despite all the discrepancies, the HONO mixing ratios agree relatively

349   well with the observed HONO mixing ratios during the period of the KORUS-AQ campaign.

350
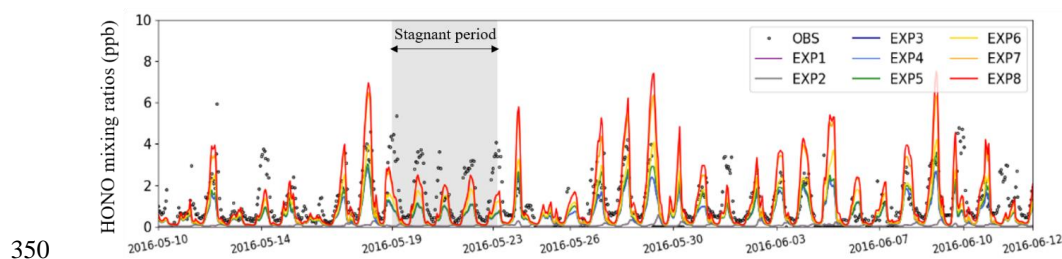
Figure 2. Hourly variations of the HONO mixing ratios (unit: ppb) at the Olympic Park station
in Seoul. The observations are marked with black circles and the colored lines represent the
HONO mixing ratios obtained from the 8 experimental simulations.

354   Figure 3 shows the diurnal variations of averaged HONO mixing ratios estimated from

355   the 8 EXP simulations, together with HONO observations at the Olympic Park station. For the

356   analysis of Fig. 3, daytime and nighttime are defined as 06:00–18:00 and 18:00–06:00 local

357   standard time, respectively. The EXP1 simulation showed slightly elevated HONO mixing

358   ratios during the daytime (purple line in Fig. 3) due to the net production of HONO in the gas

359   phase. The peak mixing ratio of the simulated HONO is ~0.14 ppb, which is significantly lower

360   than the observed mixing ratio. The large differences between EXP1 results and observations

361   suggest that there should be more unaccountable sources of HONO, which should be further

362   taken into account in our model simulations.

363   In the EXP2 simulation, HONO emissions from biomass burning were added.

364   However, the addition of these biomass burning emissions resulted in nearly negligible impact

365   on the HONO mixing ratios, because no major biomass-burning events occurred in South

366   Korea during the period of the KORUS-AQ campaign (refer to Fig. 1b). Thus, there are

367   minimal differences between the EXP1 and EXP2 simulations (i.e., between the purple and

368   grey lines in Fig. 3).

369   EXP3 simulation was then carried out to examine the impact of traffic sources (TRAF)

370   on HONO mixing ratios. The average HONO mixing ratio increases to ~0.55 ppb. As

371   previously discussed in Fig. 1c, HONO emissions from traffic sources can be significant,

372   particularly in the Seoul Metropolitan Area. However, simulated levels of HONO are still much

373   lower than observed levels of HONO.

374   HONO emissions from soil (SOIL) were further included in the EXP4 simulation. As

375   discussed previously, several studies have reported that the consideration of soil emissions can

376   lead to large increases in atmospheric HONO mixing ratios, particularly in East Asia (Fig. 1e).

377   However, it was found that almost no significant changes had occurred in South Korea.

378   In the EXP5 simulation, the heterogeneous reactions of NO_2 on the surfaces of

379   atmospheric aerosols (HET_A) were further taken into account. The addition of these reactions

380   was found to have only minor effect on the HONO mixing ratios, because γ_{a,NO_2} used in Eq.

381   (1) is too small to enhance the HONO mixing ratios in reaction (R5). In our study, the

382   heterogeneous reactions on the surface of atmospheric aerosols contribute only ~0.06 ppb. The

383   heterogeneous reactions can be potentially important in more polluted regions where larger

384   aerosol surface areas are available (Zhang et al., 2019).

385   On the contrary, the HONO mixing ratios can be greatly enhanced by NO_2 to HONO

386   conversions on the surfaces of the tree leaves and buildings. These two processes were

387   implemented in the EXP6 and EXP7 simulations (HET_L and HET_BD). In these two cases,

388   there were significant increases in the HONO mixing ratios, particularly during the nighttime

389   (i.e., on average, increases of 0.23 and 0.55 ppb in the HONO mixing ratios were found in the

390   EXP6 and EXP7 simulations, respectively).

391   Finally, the photolytic renoxification of nitrate was added to the EXP8 simulation. In

392   this EXP8 simulation, the averaged HONO mixing ratios increased by 0.11 ppb. The

393   enhancement in the HONO mixing ratios was particularly large in the early morning (an

394   increase of ~0.23 ppb was found at 6 a.m.). Overall, the EXP8 simulation produced the best

395   HONO mixing ratios (averaged value of 1.18 ppb), compared to observed HONO mixing ratio

396   (1.35 ppb). Also, the estimated HONO mixing ratios were more comparable than those in the

397   CTRL (original CMAQ v5.2.1) model simulation (represented by black squares in Fig. 3).

398   Again, it is noted that our simulations incorporated 'new HONO processes' such as: i) the

399   photo-enhanced HONO production pathway through (R5) and (R6); ii) daytime HONO

400   production from renoxification reactions through (R7) and (R8); and iii) HONO emissions

401   (refer to Table 1).

402   In addition to the graphical comparison in Fig. 3, several statistical metrics were also

403   calculated to evaluate the performances of the 8 EXP and CTRL simulations in Table 4.

404   Significant improvements were found when the HONO processes were sequentially added

405   from the EXP1 to the EXP8 simulations. For example, the index of agreement (IOA) increases

406   from 0.44 to 0.76, and the mean bias (MB) decreases drastically from -1.29 ppb to -0.17 ppb

407   from the EXP1 to the EXP8. In particular, the EXP8 simulation showed the best performance,

408   compared to the CTRL simulation during the daytime. For example, the IOA during the

409   daytime increased from 0.59 to 0.68, while the MB decreases from -0.57 to -0.34, respectively.

410   The root mean square error (RMSE) also decreased from 0.80 to 0.70 during the daytime.

411   Although the EXP8 simulation showed a notable enhancement in HONO production,

412   the HONO mixing ratios were still underestimated during the daytime. Such underestimation

413   of HONO mixing ratios during the daytime could be attributed to stronger HONO photo-

414   dissociation than in real situations. This is possibly due to failure in predicting cloud shades

415   fractions in meteorological modeling and/or due to additional sources that were not considered

416   in this study (e.g., acid displacement for HNO_3 and HCl) (VandenBoer et al., 2013). This

417   certainly indicates that additional work is needed to further investigate HONO formation and

418   removal during the daytime.

419
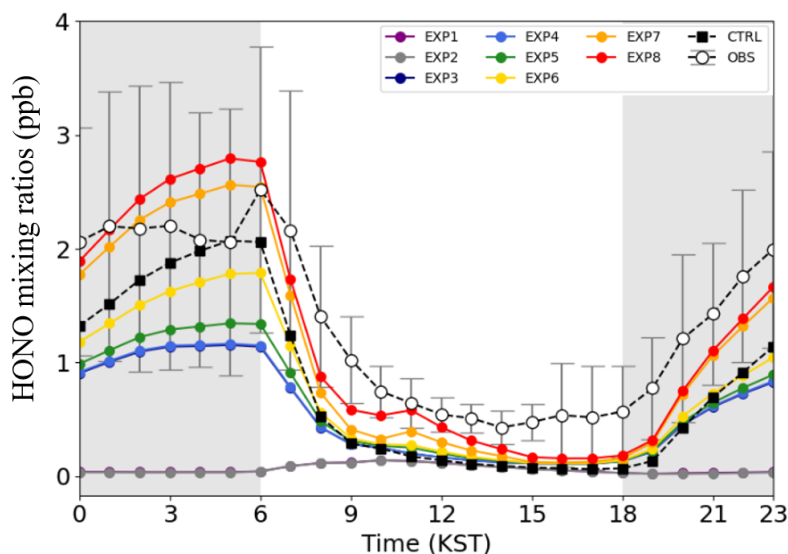
420

421   **Figure 3.** Diurnal variations of HONO mixing ratios (unit: ppb) at the Olympic Park station
422   averaged over the period of the KORUS-AQ campaign. Error bars and grey-shaded areas
423   indicate one standard deviation and nighttime (18 – 06 LST, Local Standard Time),
424   respectively.

425

426

427

428

429

430

431 **Table 4**. Statistical analysis with modeled and observed HONO mixing ratios at the Olympic
432 Park station, Seoul, Korea.

Experiment	Observed mean (ppb)	Modeled mean (ppb)	RMSE (ppb)	MB (ppb)	IOA
CTRL	1.35	0.78	1.06	-0.57	0.75
EXP1	1.35	0.06	1.68	-1.29	0.44
EXP2	1.35	0.06	1.68	-1.29	0.44
EXP3	1.35	0.55	1.15	-0.79	0.63
EXP4	1.35	0.56	1.15	-0.79	0.64
EXP5	1.35	0.61	1.12	-0.73	0.66
EXP6	1.35	0.75	1.02	-0.60	0.72
EXP7	1.35	1.07	1.05	-0.28	0.77
EXP8	1.35	1.18	1.12	-0.17	0.76

433

434 **3.2 Relative contribution of HONO sources**

435 Individual HONO processes affect the HONO mixing ratios in different ways. Figure

436 4 summarizes the relative contribution of HONO processes to the HONO mixing ratios. During

437 the daytime, both GAS and RENO$_x$ contribute significantly to the production of atmospheric

438 HONO molecules. In particular, the contribution of these two processes is the largest between

439 10:00 and 16:00 local time, when sunlight is strong. These two processes account for 29.1%

440 and 29.8% of the daytime HONO production, respectively, but are almost negligible during the

441 nighttime.

442 During the nighttime, TRAF (denoted by navy color in Fig. 4) contributes the large

443 portion of 47.2% of the total HONO production. In turn, HET_BD and HET_L exhibit

444 substantial contributions of 28.5% and 10.6%, respectively during the nighttime. The

445 contributions of other processes such as biomass burning (BioB) and heterogeneous reactions

446 on atmospheric aerosols (HET_A) are minimal. HET_A contributes only 4.3% during the

447 nighttime. Its contribution increases to 4.2% during the daytime. In terms of the average 24-

448 hour contribution, TRAF (41.4%), HET_BD (27.1%), and HET_L (11.1%) are the large

449 sources of atmospheric HONO at the Olympic Park station.

450   Using the same approach, we analyzed the HONO source contributions across South

451   Korea during the period of the KORUS-AQ campaign. As shown in Fig. 5f and 5c, HET_L

452   and TRAF were modeled to have the largest impacts on HONO production, contributing 0.15

453   ppb (41.5%) and 0.08 ppb (18.1%), respectively, across South Korea (also, refer to the

454   incremental ratio in Fig. S4).

455   Fig. 6 shows the contributions of different sources to the HONO mixing ratios at 8

456   super monitoring stations. As shown in Fig. 6, each station has different characteristics in terms

457   of source contribution. In particular, the contribution of HET_L at the Daejeon is 44.4%. Also,

458   TRAF in Bulkwang, Olympic Park, Mt.Taehwa, Ulsan, and Gwangju have large contributions

459   of 41.2%, 41.4%, 29.3%, 29.6%, and 40.5%, respectively. As for TRAF and HET_BD, their

460   contributions are high only in densely populated cities (refer to Fig. 5c and 5g). On the other

461   hand, the contributions of BioB, SOIL, HET_A, and $RENO_x$ sources were insignificant, as

462   shown in Fig. 5b, 5d, 5e, and 5h.

463   Meanwhile, at the Bangnyung and Jeju stations, $RENO_x$ has the largest contribution

464   of 70.4%, and 33.2%, respectively. This is because the amounts of NO_2 and HONO from direct

465   emissions (BioB, TRAF, and SOIL) are relatively small. The Bangnyung and Jeju stations are

466   located on remote and less populated islands.
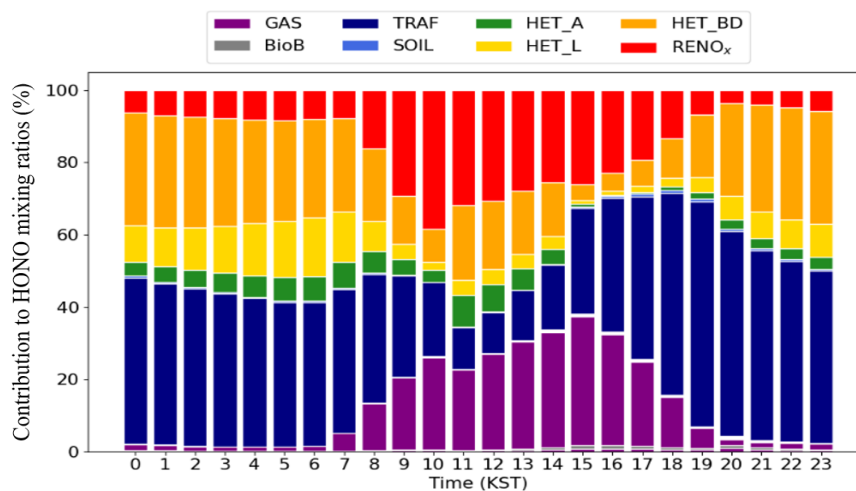
Figure 4. Diurnal contributions of individual HONO processes to the HONO mixing ratios at the Olympic Park station during the period of the KORUS-AQ campaign.
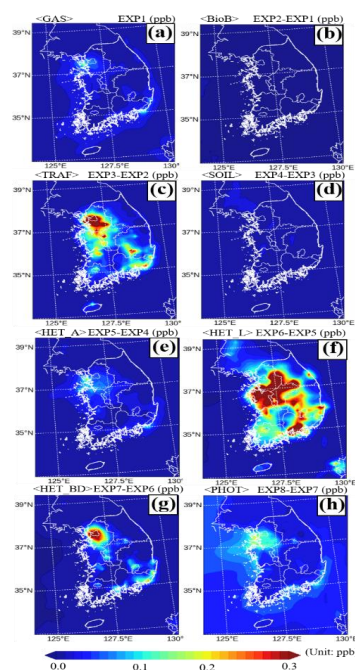
Figure 5. Spatial impacts of (a) gas phase reactions; (b) biomass burning emissions; (c) traffic emissions and (d) soil emissions; (e) heterogeneous reactions on the aerosol surfaces, (f) heterogeneous reactions on the leaf surfaces, and (g) heterogeneous reactions on the building surfaces; and (h) renoxification on HONO mixing ratios, based on model simulations during the period of the KORUS-AQ campaign in South Korea.

476
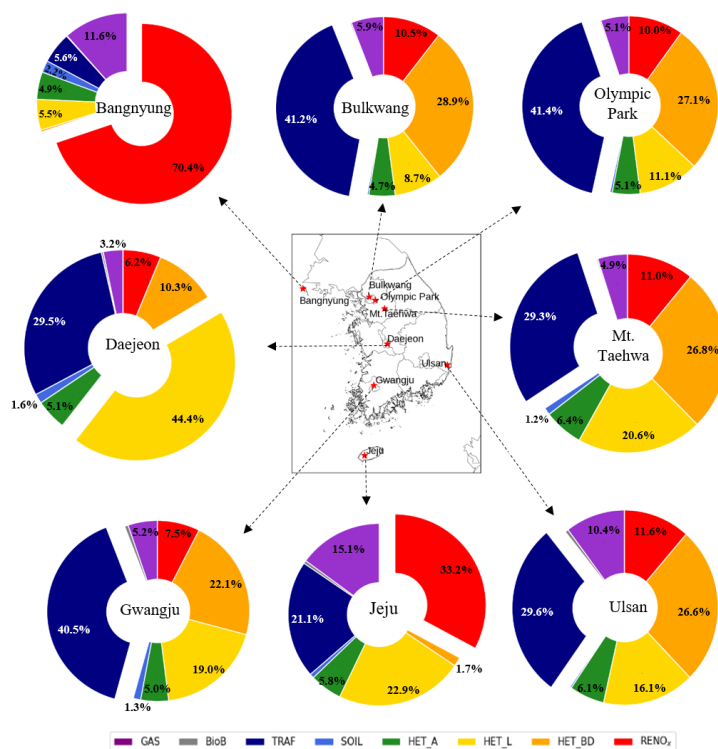
Figure 6. Contributions of individual processes to the average HONO mixing ratios at 8 monitoring stations during the period of the KORUS-AQ campaign.

479 **3.3 Impact of HONO processes on atmospheric species**

480 **3.3.1 Impact on atmospheric species**

481   We also investigated the effect of HONO processes on atmospheric levels of HO_x

482 (=$OH + HO_2$), HCHO, O_3, NO, and $PM_{2.5}$ at the Olympic Park station. Figure 7 presents the

483 diurnal concentrations of these gaseous and particulate species at the Olympic Park station.

484 The mixing ratios of OH and HO_2 radicals in the EXP8 simulation increased by 0.02 ppt (35.2%)

485 and 0.23 ppt (39.2%), respectively, compared to those in the CTRL simulation. This is certainly

486 due to the enhancement in OH levels due to HONO photo-dissociation, and then HO_2 levels in

487 the HO_x cycle. As shown in Fig. 7a (and 7b), the OH (and HO_2) mixing ratios increased from

488 0.21 ppt to 0.29 ppt (1.71 ppt to 2.28 ppt) at 1 p.m. local standard time. Subsequently, the

489   HCHO mixing ratios were also enhanced by 0.18 ppb (8.8%), due to increased VOC oxidation

490   resulting from elevated levels of OH radicals (Fig. 7c). On the contrary, the NO mixing ratios

491   in the EXP8 simulation decreased by 2.13 ppb (20.1%). This may be due to an increase in the

492   mixing ratios of HO_2 and RO_2 radicals (organic peroxyl radicals) reacting with NO molecules

493   (Fig. 7d). In other words, the reduced levels of NO indicate active NO to NO_2 conversion via

494   $NO+HO_2$ and $NO+RO_2$ reactions. Such active NO to NO_2 conversion increases the mixing

495   ratio of atmospheric ozone because these two reactions are rate-determining reactions for ozone

496   production. This is presented in Fig. 7e. In Fig. 7e, the modeled ozone mixing ratios increased,

497   approaching the observed ozone mixing ratios. This is another good result showing that the

498   incorporation of atmospheric HONO processes may be able to enhance the accuracy of

499   prediction of ozone mixing ratios. More details about ozone production are discussed in Sect.

500   3.3.2.

501   Elevated levels of atmospheric O_3 and HO_x can change the rates of particulate nitrate

502   and sulfate production. In particular, the formation of particulate nitrates and sulfates can also

503   be enhanced by increasing the levels of HNO_3, N_2O_5, and H_2SO_4. In addition, the nitrate

504   concentration can also be enhanced by the HONO reaction (i.e., via $NO_2 + H_2O \rightarrow H^+ + NO_3^-$

505   + HONO, as accounted for by R5) during the nighttime. In total, the addition of HONO

506   processes increases $PM_{2.5}$ by 4.19 μg m^{-3} (18.6%) at the Olympic Park station. However, $PM_{2.5}$

507   in the EXP8 simulation was still underestimated by 3.16 μg m^{-3} at the Olympic Park station, as

508   shown in Fig. 7f. There are several potential reasons for this underestimation, such as the

509   underestimation of secondary organic aerosol (SOA) formation (e.g., Murphy et al., 2017).

510   This issue may require further investigation in the future.

511   Figure S3 presents similar results for 320 AIR KOREA monitoring stations in South

512   Korea. The impacts of HONO processes on atmospheric levels of OH, HO_2, O_3, and $PM_{2.5}$ are

513   also presented in Fig. S4. Overall, we found that incorporating HONO chemistry into the

514   modeling system tends to enhance the mixing ratios of HO_x, which in turn increases the mixing

515   ratios of O_3 and $PM_{2.5}$.

516
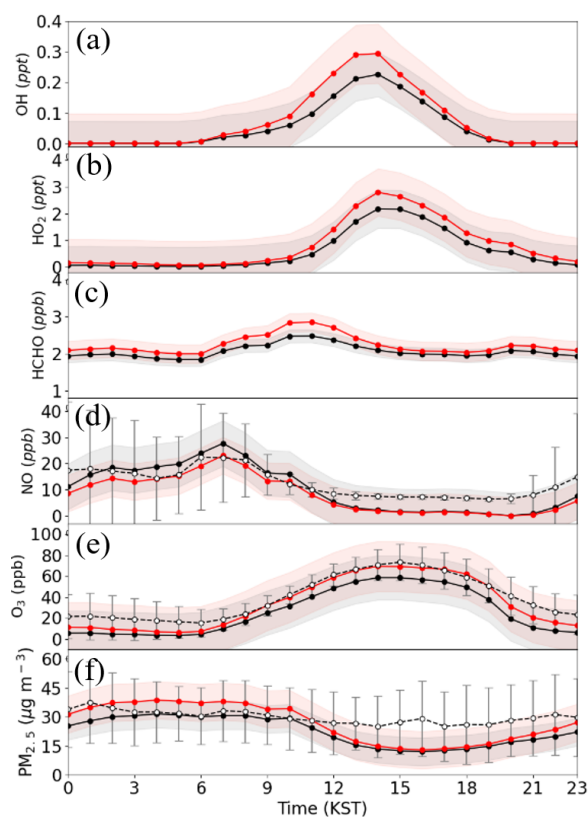
Figure 7. Diurnal variations of the mixing ratios of (a) OH, (b) HO_2, (c) HCHO, (d) NO, (e)
O_3, and (f) $PM_{2.5}$ (black lines represent the mixing ratios from the CTRL simulation and the
red lines represent those from the EXP8 simulation) and observations (marked with white open
cycles) at the Olympic Park station during the period of the KORUS-AQ campaign. Shaded
areas represent one standard deviation for each simulation.

522   **3.3.2 Impact on net ozone production**

523   The ozone mixing ratio is determined by the balance between ozone formation and

524   destruction in the atmosphere. To better understand the impacts of HONO chemistry on ozone

525   production, we quantitatively analyze the rate of net ozone production ($P(O_3)$). The $P(O_3)$ is

526   defined by equation (7):

527   P(O$_3$) = F(O$_3$) – D (O$_3$)   (Eq. 7)

528   where, F(O$_3$) and D(O$_3$) represent the rate of ozone formation and destruction, respectively.

529   F(O$_3$) and D(O$_3$) can be calculated from equations (8) and (9), respectively (Mazzuca et al.,

530   2016; Song et al., 2003).

531   F(O$_3$) = k_{HO_2+NO}[HO$_2$][NO] + k_{RO_2+NO}[RO$_2$][NO]   (Eq. 8)

532   D(O$_3$) = k_{NO_2+OH}[NO$_2$][OH] + k_{O_3+VOC}[O$_3$][VOC] + $k_{O(1D)+H_2O}$[O(^{1}D)][H$_2$O]

533   + k_{O_3+OH}[O$_3$][OH] + $k_{O_3+HO_2}$[O$_3$][HO$_2$] + $k_{RO_2+NO_2}$[RO$_2$][NO$_2$]

534   + 2k_{NO_3+VOC}[NO$_3$][VOC] + 3k_{het}[N$_2$O$_5$]   (Eq. 9)

535   where k_i represents the reaction rate constants for each reaction i. In particular, k_{het} denotes the

536   heterogeneous reaction rate constants of N$_2$O$_5$ radicals.

537   Figure 8a shows the diurnal variations of F(O$_3$), D(O$_3$), and P(O$_3$) from the CTRL and

538   EXP8 simulations. Including HONO processes in the EXP8 simulation resulted in an average

539   P(O$_3$) that was 10.6% higher than in the CTRL simulation. This is the primary reason for the

540   ozone enhancement in Fig. 7e.

541   Figures 8b and 8c provide more details about the budget of ozone production. The

542   main increase in F(O$_3$) occurred through the reactions of HO$_2$ + NO and RO$_2$ + NO. On the

543   other hand, the increase in D(O$_3$) was mainly controlled by the NO$_2$ + OH reaction at the

544   Olympic Park station. The increases in the HO$_2$ + NO and RO$_2$ + NO reaction rate exceeded

545   the increases in the reaction rate of NO$_2$ + OH, leading to the net positive ozone production

546   (i.e., positive P(O$_3$)) shown in Fig. 8a.
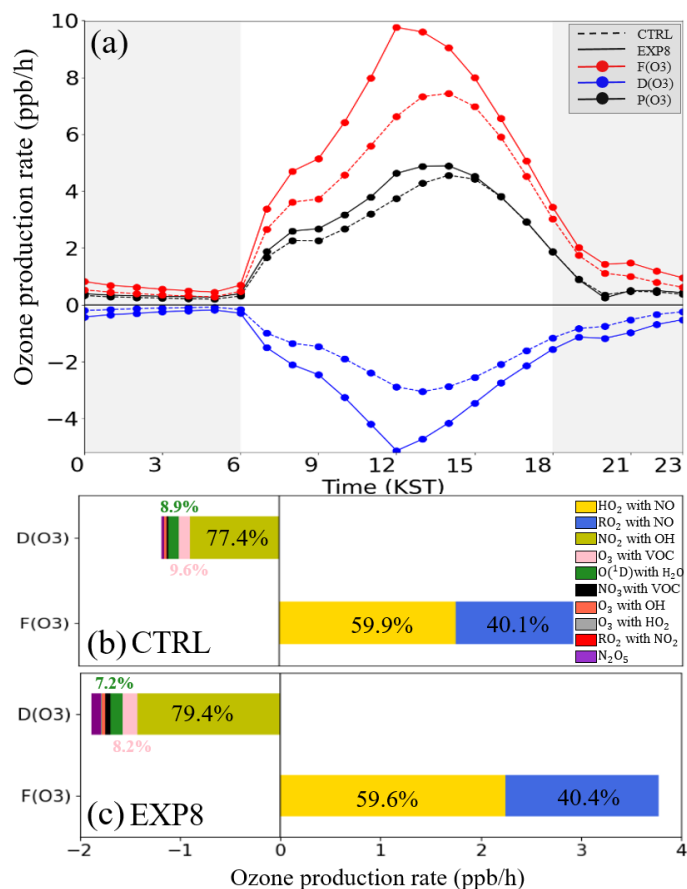
Figure 8. Diurnal variations of (a) net ozone production rate (P(O₃); black line), ozone formation rate (F(O₃); red line), and ozone loss rate (D(O₃); blue line). The dashed and solid lines represent the CTRL and EXP8 simulations, respectively. Cumulative bar chart for D(O₃) and F(O₃) in case of (b) CTRL and (c) EXP8 simulations at the Olympic Park station during the period of the KORUS-AQ campaign.

4. Conclusions

In this study, we successfully incorporated the following HONO processes into the CMAQ modeling framework to enhance the accuracy in the predictions of HONO mixing ratios: i) gas-phase HONO reactions; ii) HONO emission from biomass burning; iii) HONO emission from traffic and soil; iv) photo-induced heterogeneous reactions on the surfaces of atmospheric aerosols, tree leaves, and buildings; and v) photolysis reactions of particulate

559   nitrate and deposited HNO_3/nitrate. The analysis showed that the incorporation of HONO

560   processes into the CMAQ model framework increased the average HONO mixing ratios from

561   0.78 ppb to 1.18 ppb compared to the CTRL simulation. Average mixing ratios of HONO and

562   its diurnal patterns became much more comparable to observations, with large improvements

563   in statistical parameters. Especially during the daytime, IOA increased from 0.59 to 0.68, while

564   the MB decreased from -0.57 ppb to -0.34 ppb, and RMSE dropped from 0.80 ppb to 0.70 ppb,

565   as HONO processes were fully incorporated into the CMAQ model.

566   Several findings also emerged from the sensitivity simulations. First, each HONO process

567   had a different effect on the HONO mixing ratios during the daytime and the nighttime at the

568   Olympic Park station. For example, the GAS (29.1%) and $RENO_x$ processes (29.8%) had major

569   contributions to the mixing ratios of HONO during the daytime, while the TRAF (47.2%) and

570   HET_BD (28.5%) processes had large contributions to the mixing ratios of HONO during the

571   nighttime. During the period of the KORUS-AQ campaign, HONO mixing ratios estimated at

572   the Olympic Park station were enhanced by an average of 41.4% (TRAF), 27.1% (HET_BD),

573   and 11.1% (HET_L).

574   In the experimental simulation including all the HONO processes (i.e., EXP8 simulation),

575   the mixing ratios of OH, HO_2, HCHO, O_3, and $PM_{2.5}$ at the Olympic Park station increased by

576   0.02 ppt (35.2%), 0.23 ppt (39.2%), 0.18 ppb (8.8%), 7.86 ppb (30.8%), and 4.19 μg m^{-3}

577   (18.6%), respectively, compared to those from the CTRL simulation. The net ozone production

578   rate was enhanced by 0.19 ppb h^{-1} (10.6%) with the EXP8 simulation. This increases in $P(O_3)$

579   were caused mainly by the increased reaction rates of HO_2 + NO.

580   In this study, we improved our understanding of atmospheric HONO processes in

581   South Korea. Nevertheless, we believe that both further field studies and modeling

582   investigations are necessary for many remaining HONO-related issues such as NO_2 uptake

583 coefficient, possible missing HONO sources, and daytime photochemical reaction pathways of

584 HONO. Such studies will also help to further improve the performances of current CTMs.

585   For example, the Airborne and Satellite Investigation of Asian Air Quality (ASIA-AQ)

586 field campaign organized by the National Institute of Environmental Research (NIER) in Korea

587 and the National Aeronautics and Space Administration (NASA) in the U.S. is planned in 2024

588 in South Korea. In this campaign, the HONO mixing ratios are scheduled to be measured in

589 the aircraft and at the ground station. This joint campaign is thus expected to provide a valuable

590 opportunity to expand our knowledge on atmospheric HONO processes and HONO photo-

591 chemistry.

592

593 **Code and data availability**

594 After user registration, the WRF model 3.8.1 (https://www2.mmm.ucar.edu/wrf/users, last access: 11
595 April 2024) and CMAQ v5.2.1 (https://doi.org/10.5281/zenodo.1212601, last access: 11 April 2024)
596 are available from web page. The observation data we used can be accessed at https://www-
597 air.larc.nasa.gov/cgi-bin/ArcView/korusaq?GROUND-NIER-OLYMPIC-PARK=1 (last access: 11
598 April 2024).

599

600 **Author contribution**

601 **KYK** designed experiments and led manuscript writing and conceptualization. **KMH** and **CHS**
602 supervised this project and contributed to experimental design and manuscript writing. **HJL, RB,**
603 **JHY, GY,** and **BYK** performed research development. **JM** contributed to editing and writing review.
604 **JHW** and **SJC** provided useful datasets.

605

606 **Competing interests**

607 Chul H. Song is a member of the editorial board of *Atmospheric Chemistry and Physics*. The authors
608 declare that they have no conflict of interest.

609

610 **Acknowledgement**

611 This work was supported by the FRIEND (Fine Particle Research Initiative in East Asia Considering
612 National Differences) Project through the National Research Foundation of Korea funded by the
613 Ministry of Science and ICT (grant number: 2020M3G1A1114617). This work was also supported by
614 the National Research Foundation of Korea (NRF) grand funded by the Korea government (MSIT)
615 (grant number: 2021R1A2C1006660).

616

References

Acker, K., Möller, D., Wieprecht, W., Meixner, F.X., Bohn, B., Gilge, S., Plass-Dülmer, C., Berresheim, H., 2006. Strong daytime production of OH from HNO2 at a rural mountain site. Geophysical Research Letters 33.

Alicke, B., Geyer, A., Hofzumahaus, A., Holland, F., Konrad, S., Pätz, H., Schäfer, J., Stutz, J., Volz-Thomas, A., Platt, U., 2003. OH formation by HONO photolysis during the BERLIOZ experiment. Journal of Geophysical Research: Atmospheres 108, PHO 3-1-PHO 3-17.

An, J., Li, Y., Chen, Y., Li, J., Qu, Y., Tang, Y., 2013. Enhancements of major aerosol components due to additional HONO sources in the North China Plain and implications for visibility and haze. Advances in Atmospheric Sciences 30, 57-66.

Binkowski, F.S., Roselle, S.J., 2003. Models-3 Community Multiscale Air Quality (CMAQ) model aerosol component 1. Model description. Journal of geophysical research: Atmospheres 108.

Burkholder, James B., R. A. Cox, and A. R. Ravishankara. "Atmospheric degradation of ozone depleting substances, their substitutes, and related species." Chemical Reviews 115.10 (2015): 3704-3759.

Burkholder, J. B., Sander, S. P., Abbatt, J. P. D., Barker, J. R., Cappa, C., Crounse, J. D., ... & Wine, P. H. (2020). Chemical kinetics and photochemical data for use in atmospheric studies; evaluation number 19. Pasadena, CA: Jet Propulsion Laboratory, National Aeronautics and Space Administration, 2020.

Byun, D., Schere, K.L., 2006. Review of the governing equations, computational algorithms, and other components of the Models-3 Community Multiscale Air Quality (CMAQ) modeling system.

Carter, W.P., 2010. Development of the SAPRC-07 chemical mechanism. Atmospheric Environment 44, 5324-5335.

Chen, F., Dudhia, J., 2001. Coupling an advanced land surface–hydrology model with the Penn State–NCAR MM5 modeling system. Part I: Model implementation and sensitivity. Monthly weather review 129, 569-585.

Chen, Q., Edebeli, J., McNamara, S.M., Kulju, K.D., May, N.W., Bertman, S.B., Thanekar, S., Fuentes, J.D., Pratt, K.A., 2019. HONO, Particulate Nitrite, and Snow Nitrite at a Midlatitude Urban Site during Wintertime. ACS Earth and Space Chemistry 3, 811-822.

Cheng, Z., Wang, S., Fu, X., Watson, J.G., Jiang, J., Fu, Q., Chen, C., Xu, B., Yu, J., Chow, J.C., 2014. Impact of biomass burning on haze pollution in the Yangtze River delta, China: a case study in summer 2011. Atmospheric Chemistry and Physics 14, 4573-4585.

Colussi, A.J., Enami, S., Yabushita, A., Hoffmann, M.R., Liu, W.-G., Mishra, H., Goddard III, W.A., 2013. Tropospheric aerosol as a reactive intermediate. Faraday Discussions 165, 407-420.

Crawford, J. H., Ahn, J. Y., Al-Saadi, J., Chang, L., Emmons, L. K., Kim, J., ... & Kim, Y. P. (2021). The Korea–United States air quality (KORUS-AQ) field study. Elem Sci Anth, 9(1), 00163.

Crutzen, P.J., Andreae, M.O., 1990. Biomass burning in the tropics: Impact on atmospheric chemistry and biogeochemical cycles. Science 250, 1669-1678.

Czader, B., Rappenglück, B., Percell, P., Byun, D., Ngan, F., Kim, S., 2012. Modeling nitrous acid and its impact on ozone and hydroxyl radical during the Texas Air Quality Study 2006. Atmospheric Chemistry & Physics Discussions 12.

Czader, B.H., Choi, Y., Li, X., Alvarez, S., Lefer, B., 2015. Impact of updated traffic emissions on HONO mixing ratios simulated for urban site in Houston, Texas. Atmospheric Chemistry and Physics 15, 1253.

Fu, X., Wang, T., Zhang, L., Li, Q., Wang, Z., Xia, M., Yun, H., Wang, W., Yu, C., Yue, D., 2019. The significant contribution of HONO to secondary pollutants during a severe winter pollution event in southern China.

Gligorovski, S., 2016. Nitrous acid (HONO): An emerging indoor pollutant. Journal of Photochemistry and Photobiology A: Chemistry 314, 1-5.

Grell, G.A., Freitas, S.R., 2014. A scale and aerosol aware stochastic convective parameterization for weather and air quality modeling. Atmos. Chem. Phys 14, 5233-5250.

Guenther, A., Jiang, X., Heald, C., Sakulyanontvittaya, T., Duhl, T., Emmons, L., Wang, X., 2012. The Model of Emissions of Gases and Aerosols from Nature version 2.1 (MEGAN2. 1): an extended and updated framework for modeling biogenic emissions.

665   Gutzwiller, L., Arens, F., Baltensperger, U., Gäggeler, H.W., Ammann, M., 2002. Significance of semivolatile
666   diesel exhaust organics for secondary HONO formation. Environmental science & technology 36, 677-682.
667   Han, C., Yang, W., Yang, H., Xue, X., 2017. Enhanced photochemical conversion of NO2 to HONO on humic
668   acids in the presence of benzophenone. Environmental Pollution 231, 979-986.
669   Hao, Q., Jiang, N., Zhang, R., Yang, L., Li, S., 2020. Characteristics, sources, and reactions of nitrous acid during
670   winter at an urban site in the Central Plains Economic Region in China. Atmospheric Chemistry and Physics
671   20, 7087-7102.
672   Harris, G.W., Carter, W.P., Winer, A.M., Pitts, J.N., Platt, U., Perner, D., 1982. Observations of nitrous acid in the
673   Los Angeles atmosphere and implications for predictions of ozone-precursor relationships. Environmental
674   science & technology 16, 414-419.
675   Hendrick, F., Müller, J.-F., Clémer, K., Wang, P., De Mazière, M., Fayt, C., Gielen, C., Hermans, C., Ma, J., Pinardi,
676   G., 2014. Four years of ground-based MAX-DOAS observations of HONO and NO2 in the Beijing area.
677   Hong, S.-Y., Lim, J.-O.J., 2006. The WRF single-moment 6-class microphysics scheme (WSM6). Asia-Pacific
678   Journal of Atmospheric Sciences 42, 129-151.
679   Hong, S.-Y., Noh, Y., Dudhia, J., 2006. A new vertical diffusion package with an explicit treatment of entrainment
680   processes. Monthly weather review 134, 2318-2341.
681   Hou, S., Tong, S., Ge, M., An, J., 2016. Comparison of atmospheric nitrous acid during severe haze and clean
682   periods in Beijing, China. Atmospheric environment 124, 199-206.
683   Hutzell, W., Luecken, D., Appel, K., Carter, W., 2012. Interpreting predictions from the SAPRC07 mechanism
684   based on regional and continental simulations. Atmospheric Environment 46, 417-429.
685   Iacono, M.J., Delamere, J.S., Mlawer, E.J., Shephard, M.W., Clough, S.A., Collins, W.D., 2008. Radiative forcing
686   by long-lived greenhouse gases: Calculations with the AER radiative transfer models. Journal of Geophysical
687   Research: Atmospheres 113.
688   Jia, C., Tong, S., Zhang, W., Zhang, X., Li, W., Wang, Z., Wang, L., Liu, Z., Hu, B., Zhao, P., 2020. Pollution
689   characteristics and potential sources of nitrous acid (HONO) in early autumn 2018 of Beijing. Science of The
690   Total Environment 735, 139317.
691   Jiménez, P.A., Dudhia, J., González-Rouco, J.F., Navarro, J., Montávez, J.P., García-Bustamante, E., 2012. A
692   revised scheme for the WRF surface layer formulation. Monthly Weather Review 140, 898-918.
693   Jo, Y. J., Lee, H. J., Chang, L. S., & Kim, C. H. (2017). Sensitivity Study of the Initial Meteorological Fields on
694   the PM 10 Concentration Predictions Using CMAQ Modeling. Journal of Korean Society for Atmospheric
695   Environment, 33(6), 554-569.
696   Karamchandani, P., Emery, C., Yarwood, G., Lefer, B., Stutz, J., Couzo, E., Vizuete, W., 2015. Implementation
697   and refinement of a surface model for heterogeneous HONO formation in a 3-D chemical transport model.
698   Atmospheric Environment 112, 356-368.
699   Keywood, M., Selleck, P., Reisen, F., Cohen, D., Chambers, S., Cheng, M., Cope, M., Crumeyrolle, S., Dunne,
700   E., Emmerson, K., Fedele, R., Galbally, I., Gillett, R., Griffiths, A., Guerette, E.-A., Harnwell, J.,
701   Humphries, R., Lawson, S., Miljevic, B., Molloy, S., Powell, J., Simmons, J., Ristovski, Z., and Ward, J.:
702   Comprehensive aerosol and gas data set from the Sydney Particle Study, Earth Syst. Sci. Data, 11, 1883–
703   1903, https://doi.org/10.5194/essd-11-1883-2019, 2019.
704   Kim, S., VandenBoer, T.C., Young, C.J., Riedel, T.P., Thornton, J.A., Swarthout, B., Sive, B., Lerner, B., Gilman,
705   J.B., Warneke, C., 2014. The primary and recycling sources of OH during the NACHTT-2011 campaign:
706   HONO as an important OH primary source in the wintertime. Journal of Geophysical Research: Atmospheres
707   119, 6886-6896.
708   Kirchstetter, T.W., Harley, R.A., Littlejohn, D., 1996. Measurement of nitrous acid in motor vehicle exhaust.
709   Environmental science & technology 30, 2843-2849.
710   Kleffmann, J., Gavriloaiei, T., Hofzumahaus, A., Holland, F., Koppmann, R., Rupp, L., Schlosser, E., Siese, M.,
711   Wahner, A., 2005. Daytime formation of nitrous acid: A major source of OH radicals in a forest. Geophysical
712   Research Letters 32.

713   Kurtenbach, R., Becker, K., Gomes, J., Kleffmann, J., Lörzer, J., Spittler, M., Wiesen, P., Ackermann, R., Geyer,
714   A., Platt, U., 2001. Investigations of emissions and heterogeneous formation of HONO in a road traffic tunnel.
715   Atmospheric Environment 35, 3385-3394.

716   Lee, H.-J., Jo, H.-Y., Kim, J.-M., Bak, J., Park, M.-S., Kim, J.-K., Jo, Y.-J., Kim, C.-H., 2023. Nocturnal Boundary
717   Layer Height Uncertainty in Particulate Matter Simulations during the KORUS-AQ Campaign. Remote
718   Sensing 15, 300.

719   Lee, J., Whalley, L., Heard, D., Stone, D., Dunmore, R., Hamilton, J., Young, D., Allan, J., Laufs, S., Kleffmann,
720   J., 2016. Detailed budget analysis of HONO in central London reveals a missing daytime source. Atmospheric
721   Chemistry and Physics 16, 2747-2764.

722   Levy, M., Zhang, R., Zheng, J., Zhang, A.L., Xu, W., Gomez-Hernandez, M., Wang, Y., Olaguer, E., 2014.
723   Measurements of nitrous acid (HONO) using ion drift-chemical ionization mass spectrometry during the 2009
724   SHARP field campaign. Atmospheric Environment 94, 231-240.

725   Li, D., Xue, L., Wen, L., Wang, X., Chen, T., Mellouki, A., Chen, J., Wang, W., 2018. Characteristics and sources
726   of nitrous acid in an urban atmosphere of northern China: Results from 1-yr continuous observations.
727   Atmospheric Environment 182, 296-306.

728   Li, G., Lei, W., Zavala, R., Volkamer, R., Dusanter, S., Stevens, P., Molina, L.T., 2010. Impacts of HONO sources
729   on the photochemistry in Mexico City during the MCMA-2006/MILAGO Campaign.

730   Li, X., Brauers, T., Häseler, R., Bohn, B., Fuchs, H., Hofzumahaus, A., Holland, F., Lou, S., Lu, K., Rohrer, F.,
731   2012. Exploring the atmospheric chemistry of nitrous acid (HONO) at a rural site in Southern China.
732   Atmospheric Chemistry and Physics 12, 1497-1513.

733   Li, X., Rohrer, F., Hofzumahaus, A., Brauers, T., Häseler, R., Bohn, B., Broch, S., Fuchs, H., Gomm, S., Holland,
734   F., 2014. Missing gas-phase source of HONO inferred from Zeppelin measurements in the troposphere.
735   Science 344, 292-296.

736   Lu, X., Wang, Y., Li, J., Shen, L., Fung, J.C., 2018. Evidence of heterogeneous HONO formation from aerosols
737   and the regional photochemical impact of this HONO source. Environmental Research Letters 13, 114002.

738   Mazzuca, G.M., Ren, X., Loughner, C.P., Estes, M., Crawford, J.H., Pickering, K.E., Weinheimer, A.J., Dickerson,
739   R.R., 2016. Ozone production and its sensitivity to NO x and VOCs: results from the DISCOVER-AQ field
740   experiment, Houston 2013. Atmospheric Chemistry and Physics 16, 14463-14474.

741   Meusel, H., Kuhn, U., Reiffs, A., Mallik, C., Harder, H., Martinez, M., Schuladen, J., Bohn, B., Parchatka, U.,
742   Crowley, J.N., 2016. Daytime formation of nitrous acid at a coastal remote site in Cyprus indicating a common
743   ground source of atmospheric HONO and NO. Atmospheric Chemistry and Physics 16, 14475-14493.

744   Meusel, H., Tamm, A., Kuhn, U., Wu, D., Leifke, A.L., Fiedler, S., Ruckteschler, N., Yordanova, P., Lang-Yona,
745   N., Pöhlker, M., 2018. Emission of nitrous acid from soil and biological soil crusts represents an important
746   source of HONO in the remote atmosphere in Cyprus. Atmospheric Chemistry and Physics 18, 799-813.

747   Monks, P.S., Granier, C., Fuzzi, S., Stohl, A., Williams, M.L., Akimoto, H., Amann, M., Baklanov, A.,
748   Baltensperger, U., Bey, I., 2009. Atmospheric composition change–global and regional air quality.
749   Atmospheric environment 43, 5268-5350.

750   MURPHY, Benjamin N., et al. Semivolatile POA and parameterized total combustion SOA in CMAQv5. 2:
751   impacts on source strength and partitioning. *Atmospheric chemistry and physics*, 2017, 17.18: 11107-11133.

752   Nagai, K., Kubota, M., 1972. On the volatilization of nitrogen during nitrification in soils under vinyl covered
753   culture. 5. on the effects of iron complex salts and treatments with nitrates or chloride on volatilization of
754   nitrous acid. Jap J Sci Soil and Manure.

755   Nakashima, Y., Kajii, Y., 2017. Determination of nitrous acid emission factors from a gasoline vehicle using a
756   chassis dynamometer combined with incoherent broadband cavity-enhanced absorption spectroscopy. Science
757   of The Total Environment 575, 287-293.

758   Nie, W., Ding, A., Xie, Y., Xu, Z., Mao, H., Kerminen, V.-M., Zheng, L., Qi, X., Huang, X., Yang, X.-Q., 2015.
759   Influence of biomass burning plumes on HONO chemistry in eastern China. Atmospheric Chemistry and
760   Physics.

761 Oswald, R., Behrendt, T., Ermel, M., Wu, D., Su, H., Cheng, Y., Breuninger, C., Moravek, A., Mougin, E., Delon,
762   C., 2013. HONO emissions from soil bacteria as a major source of atmospheric reactive nitrogen. Science 341,
763   1233-1235.
764 Pathak, R.K., Wu, W.S., Wang, T., 2009. Summertime PM 2.5 ionic species in four major cities of China: nitrate
765   formation in an ammonia-deficient atmosphere. Atmospheric Chemistry and Physics 9, 1711-1722.
766 Rappenglück, B., Lubertino, G., Alvarez, S., Golovko, J., Czader, B., Ackermann, L., 2013. Radical precursors
767   and related species from traffic as observed and modeled at an urban highway junction. Journal of the Air &
768   Waste Management Association 63, 1270-1286.
769 Reisinger, A.R., 2000. Observations of HNO2 in the polluted winter atmosphere: possible heterogeneous
770   production on aerosols. Atmospheric Environment 34, 3865-3874.
771 Ren, X., Harder, H., Martinez, M., Lesher, R.L., Oliger, A., Simpas, J.B., Brune, W.H., Schwab, J.J., Demerjian,
772   K.L., He, Y., 2003. OH and HO2 chemistry in the urban atmosphere of New York City. Atmospheric
773   Environment 37, 3639-3651.
774 Romer, P.S., Wooldridge, P.J., Crounse, J.D., Kim, M.J., Wennberg, P.O., Dibb, J.E., Scheuer, E., Blake, D.R.,
775   Meinardi, S., Brosius, A.L., 2018. Constraints on Aerosol Nitrate Photolysis as a Potential Source of HONO
776   and NO x. Environmental science & technology 52, 13738-13746.
777 Ryu, S.Y., Kim, J.E., Zhuanshi, H., Kim, Y.J., Kang, G.U., 2004. Chemical composition of post-harvest biomass
778   burning aerosols in Gwangju, Korea. Journal of the Air & Waste Management Association 54, 1124-1137.
779 Ryu, Y.-H., et al. (2022). "Role of upwind precipitation in transboundary pollution and secondary aerosol
780   formation: A case study during the KORUS-AQ field campaign." Journal of Applied Meteorology and
781   Climatology **61**(2): 159-174.
782 Sarwar, G., Roselle, S.J., Mathur, R., Appel, W., Dennis, R.L., Vogel, B., 2008. A comparison of CMAQ HONO
783   predictions with observations from the Northeast Oxidant and Particle Study. Atmospheric Environment 42,
784   5760-5770.
785 Skamarock, W.C., Klemp, J.B., Dudhia, J., Gill, D.O., Barker, D.M., Duda, M.G., Huang, X.-Y., Wang, W., Powers,
786   J.G., 2008. G.: A description of the Advanced Research WRF version 3, NCAR Tech. Note NCAR/TN-475+
787   STR. Citeseer.
788 Song, C., Chen, G., Hanna, S., Crawford, J., Davis, D., 2003. Dispersion and chemical evolution of ship plumes
789   in the marine boundary layer: Investigation of O3/NOy/HOx chemistry. Journal of Geophysical Research:
790   Atmospheres 108.
791 Stemmler, K., Ammann, M., Donders, C., Kleffmann, J., & George, C. (2006). Photosensitized reduction of
792   nitrogen dioxide on humic acid as a source of nitrous acid. Nature, 440(7081), 195-198.
793 Stockwell, W.R., Middleton, P., Chang, J.S., Tang, X., 1990. The second generation regional acid deposition model
794   chemical mechanism for regional air quality modeling. Journal of Geophysical Research: Atmospheres 95,
795   16343-16367.
796 Su, H., Cheng, Y.F., Cheng, P., Zhang, Y.H., Dong, S., Zeng, L.M., Wang, X., Slanina, J., Shao, M., Wiedensohler,
797   A., 2008. Observation of nighttime nitrous acid (HONO) formation at a non-urban site during PRIDE-
798   PRD2004 in China. Atmospheric Environment 42, 6219-6232.
799 Svensson, R., Ljungström, E., Lindqvist, O., 1987. Kinetics of the reaction between nitrogen dioxide and water
800   vapour. Atmospheric Environment (1967) 21, 1529-1539.
801 Tao, M., Chen, L., Wang, Z., Tao, J., Su, L., 2013. Satellite observation of abnormal yellow haze clouds over East
802   China during summer agricultural burning season. Atmospheric environment 79, 632-640.
803 Tong, S., Hou, S., Zhang, Y., Chu, B., Liu, Y., He, H., Zhao, P., Ge, M., 2015. Comparisons of measured nitrous
804   acid (HONO) concentrations in a pollution period at urban and suburban Beijing, in autumn of 2014. Science
805   China Chemistry 58, 1393-1402.
806 VandenBoer, T.C., Brown, S.S., Murphy, J.G., Keene, W.C., Young, C.J., Pszenny, A., Kim, S., Warneke, C., de
807   Gouw, J.A., Maben, J.R., 2013. Understanding the role of the ground surface in HONO vertical structure:
808   High resolution vertical profiles during NACHTT-11. Journal of Geophysical Research: Atmospheres 118,
809   10,155-110,171.

Weber, B., Wu, D., Tamm, A., Ruckteschler, N., Rodriguez-Caballero, E., Steinkamp, J., Meusel, H., Elbert, W., Behrendt, T., Soergel, M., 2015. Biological soil crusts accelerate the nitrogen cycle through large NO and HONO emissions in drylands. Proceedings of the National Academy of Sciences 112, 15384-15389.

Wiedinmyer, C., Akagi, S., Yokelson, R.J., Emmons, L., Al-Saadi, J., Orlando, J., Soja, A., 2011. The Fire INventory from NCAR (FINN): A high resolution global model to estimate the emissions from open burning. Geoscientific Model Development 4, 625.

Wiedinmyer, C., Quayle, B., Geron, C., Belote, A., McKenzie, D., Zhang, X., O'Neill, S., Wynne, K.K., 2006. Estimating emissions from fires in North America for air quality modeling. Atmospheric Environment 40, 3419-3432.

Wiesen, P., Kleffmann, J., Kurtenbach, R., Becker, K.H., 1995. Mechanistic study of the heterogeneous conversion of NO 2 into HONO and N 2 O on acid surfaces. Faraday Discussions 100, 121-127.

Woo, J.-H., Choi, K.-C., Kim, H.K., Baek, B.H., Jang, M., Eum, J.-H., Song, C.H., Ma, Y.-I., Sunwoo, Y., Chang, L.-S., 2012. Development of an anthropogenic emissions processing system for Asia using SMOKE. Atmospheric environment 58, 5-13.

Woo, J.-H., Kim, Y., Kim, H.-K., Choi, K.-C., Eum, J.-H., Lee, J.-B., Lim, J.-H., Kim, J., Seong, M., 2020. Development of the CREATE Inventory in Support of Integrated Climate and Air Quality Modeling for Asia. Sustainability 12, 7930.

WU, D., DENG, L., LIU, Y., XI, D., ZOU, H., WANG, R., SHA, Z., PAN, Y., HOU, L., LIU, M., 2020. Comparisons of the effects of different drying methods on soil nitrogen fractions: Insights into emissions of reactive nitrogen gases (HONO and NO). Atmospheric and Oceanic Science Letters 13, 224-231.

Xu, Z., Liu, Y., Nie, W., Sun, P., Chi, X., Ding, A., 2019. Evaluating the measurement interference of wet rotating-denuder–ion chromatography in measuring atmospheric HONO in a highly polluted area. Atmospheric Measurement Techniques 12, 6737-6748.

Xu, Z., Wang, T., Wu, J., Xue, L., Chan, J., Zha, Q., Zhou, S., Louie, P.K., Luk, C.W., 2015. Nitrous acid (HONO) in a polluted subtropical atmosphere: Seasonal variability, direct vehicle emissions and heterogeneous production at ground surface. Atmospheric environment 106, 100-109.

Xue, C., Ye, C., Kleffmann, J., Zhang, C., Catoire, V., Bao, F., ... & Mu, Y. (2022). Atmospheric measurements at Mt. Tai–Part I: HONO formation and its role in the oxidizing capacity of the upper boundary layer. *Atmospheric Chemistry and Physics*, *22*(5), 3149-3167.

Ye, C., Gao, H., Zhang, N., Zhou, X., 2016. Photolysis of nitric acid and nitrate on natural and artificial surfaces. Environmental Science & Technology 50, 3530-3536.

Ye, C., Zhang, N., Gao, H., Zhou, X., 2017. Photolysis of Particulate Nitrate as a Source of HONO and NO x. Environmental Science & Technology 51, 6849-6856.

Yu, Chuan, et al. "Measurement of heterogeneous uptake of NO2 on inorganic particles, sea water and urban grime." Journal of Environmental Sciences 106 (2021): 124-135.

Yu, C., Huang, L., Xue, L., Shen, H., Li, Z., Zhao, M., ... & Wang, W. (2022). Photoenhanced heterogeneous uptake of NO2 and HONO formation on authentic winter time urban grime. *ACS Earth and Space Chemistry*, *6*(8), 1960-1968.

Yuan, H., Dai, Y., Xiao, Z., Ji, D., Shangguan, W., 2011. Reprocessing the MODIS Leaf Area Index products for land surface and climate modelling. Remote Sensing of Environment 115, 1171-1187.

Zhang, J., An, J., Qu, Y., Liu, X., Chen, Y., 2019. Impacts of potential HONO sources on the concentrations of oxidants and secondary organic aerosols in the Beijing-Tianjin-Hebei region of China. Science of The Total Environment 647, 836-852.

Zhang, J., Lian, C., Wang, W., Ge, M., Guo, Y., Ran, H., Zhang, Y., Zheng, F., Fan, X., Yan, C., 2022. Amplified role of potential HONO sources in O 3 formation in North China Plain during autumn haze aggravating processes. Atmospheric Chemistry and Physics 22, 3275-3302.

Zhang, L., Wang, T., Zhang, Q., Zheng, J., Xu, Z., Lv, M., 2016. Potential sources of nitrous acid (HONO) and their impacts on ozone: A WRF-Chem study in a polluted subtropical region. Journal of Geophysical Research: Atmospheres 121, 3645-3662.

859 Zhang, R., Sarwar, G., Fung, J.C., Lau, A.K., Zhang, Y., 2012. Examining the impact of nitrous acid chemistry on
860   ozone and PM over the Pearl River Delta Region. Advances in Meteorology 2012.
861 Zhang, Y., Shao, M., Lin, Y., Luan, S., Mao, N., Chen, W., Wang, M., 2013. Emission inventory of carbonaceous
862   pollutants from biomass burning in the Pearl River Delta Region, China. Atmospheric Environment 76, 189-
863   199.
864 Zhou, X., Zhang, N., TerAvest, M., Tang, D., Hou, J., Bertman, S., Alaghmand, M., Shepson, P.B., Carroll, M.A.,
865   Griffith, S., 2011. Nitric acid photolysis on forest canopy surface as a source for tropospheric nitrous acid.
866   Nature Geoscience 4, 440-443.